Acta Materialia 108 (2016) 26–35

Contents lists available at ScienceDirect

Acta Materialia

journal homepage: www.elsevier.com/locate/actamat

Full length article

Normalised model-based processing diagrams for additive layer manufacture of engineering alloys

Meurig Thomas [a, *], Gavin J. Baxter [b], Iain Todd [a]

[a] Department of Materials Science & Engineering, University of Sheffield, Sheffield S1 3JD, United Kingdom
[b] Rolls-Royce plc, Derby DE24 8BJ, United Kingdom

ARTICLE INFO

Article history:
Received 14 December 2015
Received in revised form
10 February 2016
Accepted 10 February 2016
Available online 23 February 2016

Keywords:
Additive layer manufacture
Processing diagrams
Microstructure
Titanium alloys
Mechanical properties

ABSTRACT

Additive Layer Manufacturing (ALM) is becoming a more widely accepted method for the production of near net-shape products across a range of industries and alloys. Depending on the end application, a level of process substantiation is required for new parts or alloys. Prior knowledge of the likely process parameter ranges that will provide a target region for the process integrity can save valuable time and resource during initial ALM trials. In this paper, the parameters used during the powder bed ALM process have been taken from the literature and the present study to construct normalised process maps for the ALM process by building on an approach taken by Ion et al. in the early 1990's (J.C. Ion, H.R. Shercliff, M.F. Ashby, Acta Metallurgica *et* Materialia 40 (1992) 1539–1551). These process maps present isopleths of normalised equivalent energy density (E_0^*) and are designed to provide a practical framework for comparing a range of ALM platforms, alloys and process parameters and provide *a priori* information on microstructure. The diagrams provide a useful reference and methodology to aid in the selection of appropriate processing parameters during the early development stages. This paper also applies the methodology to worked examples of Ti–6Al–4V depositions processed using different Electron Beam Melting parameters.

© 2016 Acta Materialia Inc. Published by Elsevier Ltd. This is an open access article under the CC BY license (http://creativecommons.org/licenses/by/4.0/).

1. Introduction

Additive Layer Manufacture (ALM) is an emerging near-net shape production technology that utilises a high-energy heat source (typically a laser or high-energy electron beam) to selectively melt or fuse together metallic powder to produce a three dimensional part direct from a CAD model on a layer by layer basis [1]. Powder ALM can be broadly divided into two forms; Blown Powder Direct Laser Deposition and Powder Bed Additive Manufacture [2]. In both cases, the powder is locally fused together using a moving heat source, although the delivery system for the powder differs. In Blown Powder Deposition systems [3,4], the feedstock powder is fed directly onto a work-piece using a pressurised inert gas flow, whilst in Powder Bed Additive Manufacturing systems, the feedstock powder is supplied from one or more hoppers and applied across a baseplate using a raking or rolling mechanism [5,6]. For powder bed systems, two distinct sub-categories exist; those for which the heat source used to fuse the metal powder is a laser (Laser Additive Manufacture, or Laser AM) and those which use a high-energy electron beam (Electron Beam Manufacture, or EBM).

The viability of laser-based and electron beam-based ALM has been successfully demonstrated for Titanium alloys [5,7–12], Nickel-base Alloys [2,6,13–16] and 316L Stainless Steel [17,18]. A key challenge facing researchers interested in the ALM of engineering alloys is developing the understanding of how to determine the key process variables to yield both a sound microstructure, acceptable mechanical properties and significantly reduce the probability of a finished component containing undesirable microstructural aberrations such as gas porosity, lack of fusion voids or internal cracks [10]. For example, insufficient heat-input due to high laser beam velocities is reported to introduce a high fraction of internal voids in CM247 LC by Carter et al. [2,6] and in 316L Stainless Steel by Kamath et al. [17], whilst Juechter et al. [8] were able to define an acceptable processing parameter window for Electron Beam Manufacture (EBM) of Ti–6Al–4V.

Efforts are currently underway to develop numerical models to predict void formation during Additive Manufacturing Processes [19,20], and whilst these models offer a good degree of precision,

* Corresponding author.
E-mail address: Meurig.thomas@sheffield.ac.uk (M. Thomas).

http://dx.doi.org/10.1016/j.actamat.2016.02.025
1359-6454/© 2016 Acta Materialia Inc. Published by Elsevier Ltd. This is an open access article under the CC BY license (http://creativecommons.org/licenses/by/4.0/).

they can be computationally expensive and may require extensive experimental validation. A practical alternative to numerical process modelling is the construction of empirical and physically-based process maps that can, for example, define "safe" and "unsafe" regions for hot-working [21,22], "weldable" regions for Nickel superalloys [23] or the transition from an equiaxed to columnar microstructure during solidification [24,25].

Diagrams for laser processing of engineering materials have previously been developed by Ion et al. [26], through the application of an analytical heat flow model to identify dimensionless groups of processing parameters. Experimental data were normalised against material thermophysical properties to define a set of practical operating regions for a range of CO_2 laser treatments. The advantage of this approach over, for example, that outlined by Dye et al. [23], is that instructive process maps can be rapidly produced using more straightforward mathematics, data available in the literature and readily available computer software (e.g. Microsoft Excel).

In this paper, we will firstly employ, and then extend, the approach developed by Ion et al. [26] to construct normalised process maps for ALM. We will identify dimensionless groups of process variables applicable to ALM and construct a practical, normalised process map from which informed decisions on the selection of appropriate processing parameters can be made. Such a process map is intended to provide a framework for comparing and classifying the extensive range of processing parameter data available in the literature, rather than as a predictive tool to provide *a priori* information on microstructural-scale and morphology, or the likelihood that a manufactured artefact will contain an undesirable microstructural feature.

Following this, the application of the proposed normalised process map for Electron Beam Manufacture (EBM) of the α/β Titanium alloy Ti–6Al–4V will be discussed. The effect of systematically varying the process parameters on the microstructure, microhardness and the propensity for undesirable internal features to exist within the deposit will be investigated and the results discussed within the process map framework.

2. Development of normalised process maps for Additive Layer Manufacture

A significant quantity of processing parameter data for powder bed ALM of a wide range of engineering alloys are available in the literature. Table 1 provides a non-exhaustive summary of the additive manufacturing platforms, alloys studied, the corresponding processing parameters extracted from the literature and the source from which thermophysical data were taken. From Table 1, it is evident that a range of heat sources, powder bed temperatures and processing conditions have been investigated, including beam power q, velocity v, layer thickness l, hatch spacing h and beam radius r_B. The large number of potential parameter combinations however, would make the analysis of independent effects of the on microstructure challenging. Ion et al. [26] define the following two dimensionless groups for laser processing of materials:

Dimensionless Beam Power:

$$q^* = Aq/[r_B\lambda(T_m - T_0)] \tag{1a}$$

Dimensionless Beam Velocity:

$$v^* = vr_B/\alpha \tag{1b}$$

where A is the surface absorptivity or coupling coefficient and ranges between 0.3 and 0.8 (See Table 1 in Ref. [26]), r_B is the beam radius, λ and α are the thermal conductivity and thermal diffusivity of the alloy being processed, whilst T_m and T_0 are the respective melting and initial temperatures of the material (*i.e.* the powder bed temperature in the case of the latter).

According to Ion et al. [26], q^* and v^* can be considered physically to control the peak temperature and heating rate of the thermal cycle at a point in the material. In this analysis, the average thermal properties of the alloy (λ and a) at the approximate powder bed operating temperature are used, rather than at 0.6 T_m as assumed by Ion et al., although we will also assume the thermophysical properties are unchanged by melting. The thermal properties of the powder bed will be assumed to be that of fully dense material; ideally, the thermo-physical properties of the alloy in powder form should be chosen, but data relating to bulk powder thermal properties are not as readily available as fully dense material. The surface absorptivity is assumed to remain constant at 0.5, although it is appreciated that values for A can range between 0.35 for Laser Deposition [27] and 0.55 for Electron Beam Welding [28]. The reason for this is that measured values of surface absorptivity are seldom reported by the studies listed in Table 1, and therefore the Absorptivity value for Laser Cladding suggested in Ref. [26] has been adopted. Data for q, v, and r_B are listed in Table 1.

In addition to beam power and velocity, which are typically two of the key process variables in laser welding, ALM introduces two further process variables: Layer height, l, and hatch spacing, h. As a basic approximation and with reference to Fig. 1, consider a moving heat source heating a volume of material of cross-sectional area $2r_B.l$, where l is approximated by the layer height of the powder bed, with a powder packing density of approximately 60–70% relative density. For simplicity, a powder bed relative density of 0.67 (2.d.p) will be assumed in this analysis. If the energy used per unit length of track is q/v then the energy per unit volume E, required to raise the material to a critical temperature, say the melting point T_m, is $q/2vlr_B$. In dimensionless terms, this can be written as:

$$E^* = q^*/v^*l^* = [Aq/(2vlr_B)]\left[1/0.67\rho C_p(T_m - T_0)\right] \tag{2}$$

where $l^* = 2l/r_B$ is the dimensionless layer height. Physically, the group of dimensionless parameters in Equation (2) represent the amount of energy required in a single laser scan to raise the local temperature of the powder bed to the melting temperature of the material. The minimum amount of heat to cause melting per m^3 of material, H_{min}, including the latent heat, L_m, is:

$$H_{min} = \rho C_p(T_m - T_0) + L_m \tag{3a}$$

where L_m is approximately $0.5\rho C_p(\Delta T)$ for metals and alloys and H_{min} therefore becomes

$$H_{min} \approx 1.5\rho C_p(T_m - T_0) \tag{3b}$$

Substitution of equation 3b into 2 gives:

$$E^*_{min} = q^*/v^*l^* = [Aq/(2vlr_B)]\left[1/\rho C_p(T_m - T_0)\right] \tag{4}$$

where E^*_{min} is the minimum dimensionless heat input per unit volume required to melt the material.

The Hatch Spacing, h, is an important processing parameter as it controls the amount of overlap between adjacent melt pools. Selection of a large hatch spacing lends itself to more rapid part manufacture, but potentially less re-melt overlap between adjacent scan lines (and the potential for void formation) if the beam power is not commensurately increased. Conversely, a small hatch spacing value will increase the total manufacturing time of the part, introduce more re-melting and thus redundant heat input. In keeping with the dimensionless layer height, l^*, the hatch spacing

Table 1
Summary of the Additive Layer Manufacture process parameters reported in the literature and reviewed in this study.

	Heat source (type)		Processing parameters						Thermophysical properties
	AM platform	Alloy system	Bed Temp., T_0 (K)	Power, q (W)	Velocity, v (m/s)	Layer height, l (m)	Hatch spacing, h (m)	Beam radius, r_B (m)	
This study	Electron Beam[a] *Arcam A2*	Ti–6Al–4V	923	600	–	–	–	150×10^{-6}	Al-Bermani et al. [7]
Juechter et al. [8]	Electron Beam[a] *Arcam S12*	Ti–6Al–4V	923	60–1400	0.2–6.4	50×10^{-6}	100×10^{-6}	150×10^{-6}	Al-Bermani et al. [7]
Vranken et al. [12,29]	Laser (SMYb:YAG) *In-house LM-Q*	Ti–6Al–4V	298	250	1.6	30×10^{-6}	60×10^{-6}	52×10^{-6}	ASM International [41]
Qui et al. [9],	Laser *Concept Laser M2*	Ti–6Al–4V	298	150–200	0.8–1.5	20×10^{-6}	75×10^{-6}	75×10^{-6}	ASM International [41]
Xu et al. [5]	Laser *SLM 250 HL*	Ti–6Al–4V	498	175–375	0.7–1.029	$30–90 \times 10^{-6}$	$120–180 \times 10^{-6}$	$70–120 \times 10^{-6}$	ASM International [41]
Kamath et al. [17]	Laser *Concept Laser M2*	316L SS	298	150–400	0.5–2.5	30×10^{-6}	112×10^{-6}	27×10^{-6}	ASM International [42]
Ziolkowski et al. [18]	Laser *SLM Realizer II*	316L SS	298	97	0.2	50×10^{-6}	125×10^{-6}	100×10^{-6}	ASM International [42]
Unpublished Data	Laser	Duplex SS	298	–	–	–	–	–	–
Cooper et al. [13]	Laser *In-house*	Inconel®625	298	800–1000	0.1–0.12	100×10^{-6}	500×10^{-6}	850×10^{-6}	ASM International [43]
Boswell et al. [30]	Laser *SLM 280HL*	Inconel®718	298	–	–	–	–	–	ASM International [43]
Carter et al. [2,6]	Laser *Concept Laser M2*	CM247	298	100–200	0.4–2.0	20×10^{-6}	75×10^{-6}[b]	75×10^{-6}	Mukai et al. [44] Avala et al. [45]
Boswell [30]	Laser EOS M270	CM247	298	–	–	–	–	–	Mukai et al. [44] Avala et al. [45]
Brif et al. [31]	Laser *AM 125*	FeCoCrNi	298	200	0.33–0.60	$20–50 \times 10^{-6}$	90×10^{-6}	25×10^{-6}	Brif et al. [31]

Assumed in this analysis to be equal to the parameters used by Qui et al. [9] (Experiments performed within the same research group and on the same AM Platform).
[a] Heated Powder Bed. T_0 923 K.
[b] Not provided.

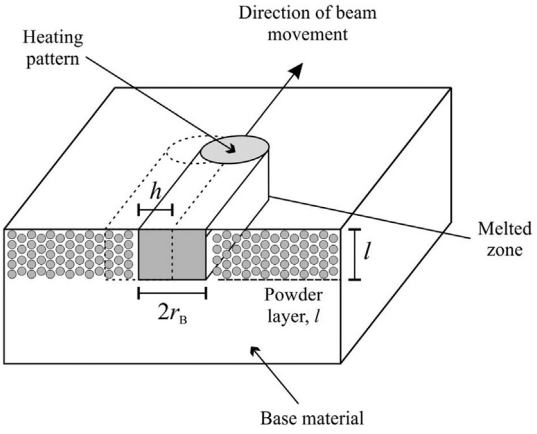

Fig. 1. Schematic illustration of the simplified melting pattern geometry for Powder Bed ALM assumed in this analysis. Adapted from Fig. 3 in Ion et al. [26].

has been normalised against the beam radius r_B to give:

$$h^* = h/r_B \tag{5}$$

The two sets of normalised parameters, the volumetric Energy Density (E^*) and hatch spacing (h^*) can be used, in conjunction with the data available in Table 1, to produce a normalised process map similar to that illustrated in Fig. 2. Here, data for E^* and $1/h^*$ are calculated from the reported parameters listed in Table 1 and are plotted on the abscissa and ordinate scale, respectively (note the $\log_{10}$ scale). The reason for plotting $1/h^*$ versus E^* rather than h^* is be discussed later. Fig. 2 represents a region of process space for the normalised variables h^* q^*, v^* and l^*, with the latter three parameters being combined into a single dimensionless group of variables. Data for Ti–6Al–4V [5,8,9,29], Nickel-base Alloys [2,6,13,30], 316 and Duplex Stainless Steel [17,18], and a FeCoCrNi High Entropy Alloy (HEA) [31] are included on the process map in Fig. 2. Practical process limits for Ti–6Al–4V [8] and CM247 [2], along with the lower bound indicating the onset of void formation in 316L Stainless Steel [17] are also appended to Fig. 2

The dimensionless group of parameters $E^* = q^*/v^*l^*$ on the abscissa represent the minimum heat required to raise the temperature of the powder bed to the melting point of the material within a single laser scan line [26] (in practice, considerable re-melting of the previous layer(s) will take place with the aim of ensuring complete fusion between the individual layers and minimise void formation). For example, if we wish to reduce build time, then it may seem convenient to simply increase the velocity of the laser beam. If it is not possible to compensate for the increase in velocity by increasing beam power to maintain a constant value for q^*/v^*l^* then, accordingly, a reduction in the layer height should be required in order to avoid the onset of void formation and a reduction in relative density (see annotations in Fig. 2.) [2,17]. At the opposite end of the spectrum, a high ratio of q^*/v^* leads to solidification cracking in certain Nickel-base superalloys due to a steep thermal

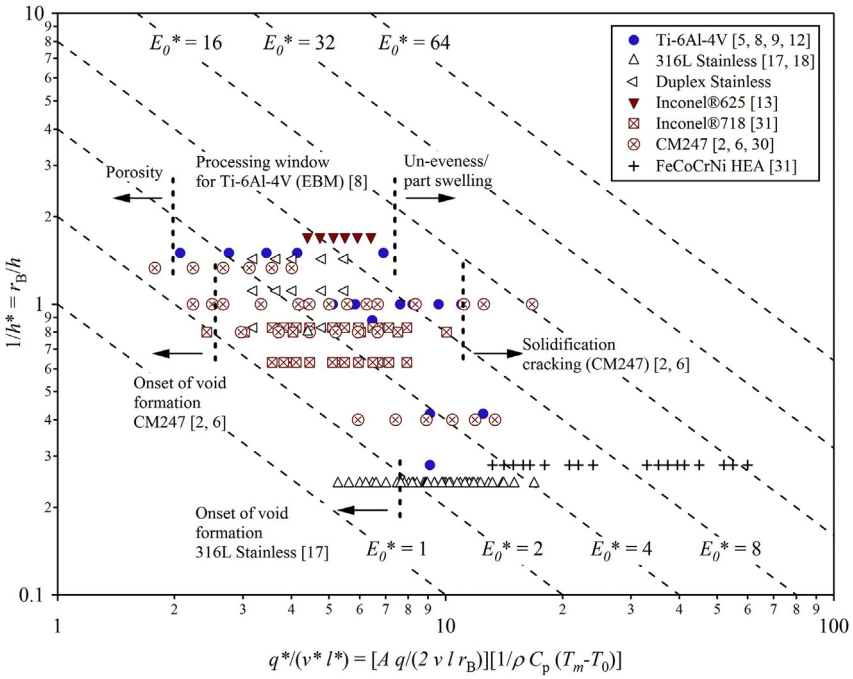

Fig. 2. Normalised processing diagram for ALM of a range of alloy systems constructed using Equation (1)–(4) and processing parameter data extracted from the literature. Contours of constant normalised equivalent energy density, E_0^*, are provided by the dashed lines and practical processing limits for Ti–6Al–4V [8], 316L Stainless Steel [17] and the Ni-alloy CM247 [2] are also annotated.

gradient G and the high volume fraction of γ' [2,6,30].

The ordinate scale, $1/h^*$, provides an indication of the magnitude of the hatch spacing relative to the laser (or electron) beam diameter, with the majority of experiments conducted in the range $0.6 < 1/h^* < 1.5$. If the magnitude of the beam radius and hatch spacing are the same, then h^* (and $1/h^*$) is equal to 1, whilst values of h^* greater than unity indicate that the hatch spacing exceeds the radius of the laser beam and *vice versa*. A large hatch spacing relative to the beam radius and/or layer height may require an either commensurate increase in beam power or reduction in beam velocity; this is to insure there is sufficient overlap between adjacent melt pools to minimise the likelihood for void formation [30]. Conversely, whilst small values of h or h^* relative to the layer height, l or l^*, may ensure a fully dense component, the increase in redundant thermal energy due to considerable re-melting across the powder bed layer may lead to a coarsening of the final microstructure.

The product of $1/h^*$ and E^* is the ratio of dimensionless volumetric heat input per scan line to the dimensionless hatch spacing, and provides us with the concept of a normalised equivalent energy density, E_0^*. Higher values of E_0^* represent a combination of process parameters that, overall, lead to excessive heat input into the powder bed, whilst insufficient heat to fully melt or fuse the feedstock powder might be expected at a lower E_0^*. Therefore, a constant value of E_0^* should provide an equally energy efficient treatment during powder bed ALM, irrespective of the individual parameters used, and isopleths of E_0^* are plotted on Fig. 2 using the following equation

$$E_0^* = q^*/v^*l^*h^* = [Aq/(2vlh)]\left[1/\rho C_p(T_m - T_0)\right] \quad (6)$$

which is proportional to the equation, $E\ q/vlh$ (J/mm^3), employed by Xu et al. [5] to understand the influence of energy density on the microstructure and properties of Ti–6Al–4V produced by selective laser melting. The first group of terms in Equation (4), $Aq/(2vlh)$, represent the key processing parameters for ALM, which are controllable and defined prior to experimentation, whilst, with the exception of the bed temperature, T_0, the second group of terms, $1/\rho C_p(T_m\text{-}T_0)$, represent the thermo-physical properties of the alloy to be fabricated.

From Fig. 2, it is evident that the majority of reported parameter combinations (listed in Table 1) fall in the range $2 < E_0^* < 8$ when normalised using Equations (1)–(6). Although a constant E_0^* suggests an equally energy efficient process, this does not imply the thermal history of a material manufactured using a range of parameter combinations that fall somewhere along an isopleth of E_0^* remains the same. For example, consider two sets of processing parameters q, v, l and h that, when evaluated using Eqn. (6), both yield $E_0^* = 6$. In the first set, a high v at a constant q and l is employed along with a small value for h to compensate for the reduced melt pool size. Under these conditions, the data point will fall in a more top-left region of the normalised process map (Fig. 2). In the second set of parameters by contrast, v is decreased to yield a larger melt and h is commensurately increased to reduce the amount of redundant work (*i.e.* large amount of re-melting) and speed the process up. Here, the data point will still fall along the $E_0^* = 6$ isopleth, but in this instance it will reside in the bottom-right region of the process map. In these situations, not only is the melt pool size likely to differ substantially, but also the melt pool geometry. As reported by Moat et al. [32], the microstructure of a laser deposited alloy, such as Waspaloy, is highly sensitive to the melt-pool geometry. As such, it is expected that the microstructure of an alloy processed via the two sets of conditions discussed with differ sharply, despite both sets providing an equally energy efficient process.

3. Application of normalised process maps for Electron Beam Manufacture of Ti–6Al–4V

Titanium alloys such as Ti–6Al–4V are an attractive class of

engineering alloy to designers due their high specific strength, good fatigue properties and excellent corrosion resistance [33,34]. Unfortunately, poor buy-to-fly ratios and high costs associated with conventional manufacturing including up-stream thermomechanical processing and machining limit their more widespread use outside high-end applications in the biomedical, petrochemical and aerospace industries. Electron Beam Melting (EBM) is an emerging additive manufacturing technology that demonstrates considerable potential for the near-net shape production of aerospace and medical components using an electron beam heat source and a heated powder bed. As per any method for the production of metallic parts, a comprehensive understanding of the processing-microstructure-property relationship is necessary in order for the technology to reach full production-level maturity [35].

The framework described in the previous section provides useful information on typical processing conditions for a range of alloys produced by ALM investigated by other researchers. Regions where either voids or internal cracks are observed are annotated on Fig. 2, but there is little information available on how microstructure varies with E_0^*. In this section and within the context of the normalised process map constructed earlier, we will investigate the effect of hatch spacing and beam velocity on the microstructure of the α/β Titanium alloy Ti–6Al–4V produced by EBM.

3.1. Experimental methods

Cuboidal specimens of dimensions 15 mm × 15 mm × 10 mm were fabricated on a 150 mm × 150 mm Ti–6Al–4V base plate using an Arcam A2 machine platform. Gas Atomised (GA) Ti–6Al–4V feedstock powder was supplied by Arcam AB, Sweden, with a Particle Size Distribution (PSD) of 45–105 μm. The nominal composition of the as-received powder is given in Table 2.

The EBM processing parameters investigated in this study are listed in Table 3 along with the normalised values calculated using Eqns. (1)–(4) in section 2. The beam power (q) was fixed at 600 W, whilst the beam velocity (v) and hatch spacing (h) were systematically varied. The layer height (l) and focus offset were kept at a constant of 0.07 mm and 19 mA, respectively. The powder bed temperature (T_0) was held at 923 K and an applied helium shielding atmosphere was operated with an over-pressure of 4×10^{-3} mbar; both of which are standard process conditions defined by Arcam for Ti–6Al–4V. In reference to the process map for ALM constructed previously (Fig. 2), the normalised parameters groups of q^*, v^*, l^* and h^* listed in Table 3 are plotted against the data from the literature in Fig. 3.

The EBM specimens were sectioned with a low speed precision cut-off wheel and prepared for metallurgical evaluation in line with the methods described by Thomas et al. [36]. Samples were initially planar ground using water-lubricated SiC paper and a 9 μm diamond suspension was employed for the final grinding step. Final polishing of the specimens was performed using colloidal silica suspension and microstructural characterisation was performed using polarised light microscopy. A circular intercept method was employed to quantify the microstructural unit size, considered to be the width of similarly orientated secondary alpha-laths, and a minimum of six circular intercept measurements were taken per specimen giving an average of over 100 lath widths. The population of internal microstructural anomalies was measured by examining six regions of interest per specimen to provide a total field of analysis of 25.2 mm^2. The size and morphology of the internal anomalies was quantified through an automated greyscale threshold procedure within the image analysis software ImageJ [37].

To obtain useful information on the likely mechanical properties, hardness testing was performed using a Struers Durascan automated hardness testing instrument with a Vickers indent of 1 kg f and a dwell time of 3 s. A total of twelve indent measurements were made per specimen, with a minimum spacing between indents of 0.5 mm.

Table 2
Nominal composition (wt. %) of the atomised Ti–6Al–4V feedstock powder.

Al	V	Fe	C	O	N	H	Ti
6.4	3.88	0.18	0.01	0.136	0.02	0.004	Bal.

3.2. Results & discussion

The effect of h^* and v^* on the microstructure of EBM Ti–6Al–4V is shown in Fig. 4. Within the context of this study, the effect of the h^* on the coarseness of the $\beta \rightarrow \alpha$ transformation product is more clearly pronounced than that of v^*. In the range $3 < E_0^* < 5$ (Fig. 4 c to j), rapid cooling through the $\beta \rightarrow \alpha + \beta$ transformation temperature results in a fine, Widmanstätten α morphology and this is consistent with the microstructures reported for ALM Ti–6Al–4V by other researchers [5,7,35]. This is in contrast with the α-colony type microstructures typically associated with slow to medium-cooled ($\alpha + \beta$) Titanium alloys [38,39].

Above $E_0^* = 6$ however, a more coarse $\alpha + \beta$ microstructure is observed (Fig. 4 a) and b)). Here, the microstructure consists of small packets of similarly orientated α laths and is more comparable to the colony microstructure observed in slow to medium cooled $\alpha + \beta$ titanium alloys manufactured through a conventional ingot metallurgical route. This is particularly the case when h^* is set to a minimum value of 0.67. Under these processing conditions, the hatch spacing is small relative to the beam diameter; hence the low values of h^* result in an overall increase in E_0^* as the process is less thermally efficient. The decrease in h^* will also lead to a slower cooling rate, due to the more closely spaced thermal gyrations [14], and such a shallower approach to the β-transus results in a smaller number of variants being selected during the $\beta \rightarrow \alpha$ phase transformation [40].

The relationship between v^*, h^* and the corresponding Vickers hardness number (VHN) is illustrated in Fig. 5. For the specimens where h was systematically varied, data on the microstructural unit size are also included. An increase of the beam traverse rate from $v^* = 23.7$ to 32.6 leads to a negligible change in the average VHN measured, although an increase in the scatter of the hardness is apparent, particularly at $v^* = 31.3$ and above. In agreement with the microstructural observations shown in Fig. 3, h^* appears to be the principal factor controlling the hardness of the alloy, with a modest overall reduction in the material hardness occurring at lower values. Material manufactured at the baseline setting; $h^* = 1.33$ and $v^* = 23.7$ yield a mean hardness value of 346 ± 4 VHN whilst reducing the magnitude of h^* to 0.67 results in a mean hardness of 327 ± 5 VHN.

The reduction in VHN associated with lower h^* values can be largely ascribed to the coarser microstructures discussed above. As the number of structural boundaries per unit volume of material is decreased (*i.e.* a larger grain size), the distance over which dislocation glide can occur before reaching a grain boundary, is increased. This leads to a reduction in the strength of the material and is reflected by the lower Vickers hardness a summarised by the Hall-Petch plot in Fig. 6.

In addition to microstructure, the presence of undesirable internal features (such as lack of fusion defects and gas porosity) in EBM Ti-6AL-4V will strongly influence mechanical performance and, as such, the feature population as a function of beam velocity and hatch offset has also been investigated. Fig. 7 illustrates an

Table 3
List of process parameters investigated for the fabrication of Ti–6Al–4V specimens via Electron Beam Additive Manufacture. T_0 923 K.

Power		Velocity	Layer height	Hatch spacing	Energy density	
q (W)	q^*	v^*	l^*	h^*	$E^* = q^*/(v^* h^*)$	$E_0{}^* = q^*/(v^* h^* l^*)$
600	71.54	23.7	0.47	1.33	1.33	4.85
600	71.54	26.2	0.47	1.33	1.33	4.38
600	71.54	28.8	0.47	1.33	1.33	3.99
600	71.54	31.3	0.47	1.33	1.33	3.67
600	71.54	32.6	0.47	1.33	1.33	3.53
600	71.54	23.7	0.47	0.67	0.67	9.71
600	71.54	23.7	0.47	1.00	1.00	6.47
600	71.54	23.7	0.47	1.67	1.67	3.88
600	71.54	23.7	0.47	2.00	2.00	3.24

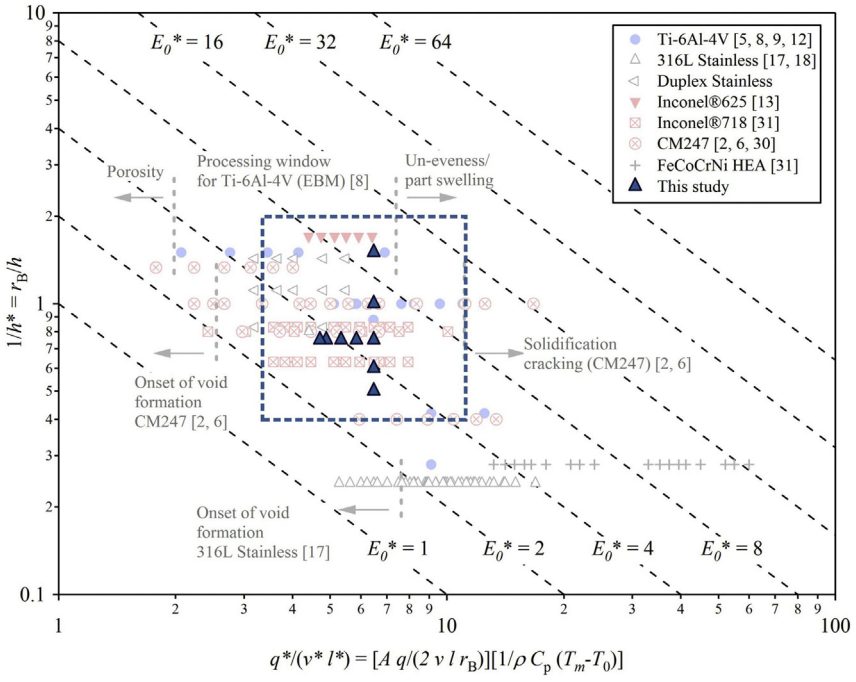

Fig. 3. Normalised processing diagram showing the location of the experimental processing parameters selected for EBM of Ti–6Al–4V in this study.

extreme example of the size and morphology of features observed within EBM material processed with $h^* = 2$ and $v^* = 23.7$. Two classes of feature can generally be identified: Large (typically >100 μm), irregular-shaped features that are likely to occur due to insufficient fusion during the melt process and spherical gas pores (typically <100 μm) that pre-exist within the gas atomised feedstock powder.

To quantify the size distribution and morphology of the observed features, an automated image thresholding technique was employed using the image analysis software ImageJ. Feature size was determined by fitting an ellipse to defects identified during the image thresholding step, with the size being defined by the length of the ellipse major axis. The morphology of the defect is defined as a measure of defect Circularity Index, C.I [37]:

$$C.I. = (4\pi A_F)\Big/(P_F)^2 \quad (7)$$

where A_F is the cross-section area of a given microstructural feature and P_F is the perimeter. A C.I. of 1 implies a perfectly spherical pore when viewed under metallographic cross-section, whilst more irregular-shaped features will possess a lower C.I. Fig. 7 is an absolute frequency histogram of the number of feature detected across a constant area of analysis of 25.2 mm^2 and shows the manner in which the size and morphology of defects changes accordingly with v^* and h^*.

It is evident from Fig. 7 that increasing both h^*, and, to a lesser extent, v^*, leads to a commensurate rise in the number of features observed in the material. In addition to an overall increase in the area density of features, morphological changes also occur, with an increase in the propensity for irregular-shaped melt features (circularity index <0.7) to be present when large h^* and v^* values are selected. The smallest number of defects is observed when h^* is set to the minimum value within the parameter space investigated for this study of 0.67 ($1/h^* = 1.5$ to 1 decimal place). At this setting, no irregular-shaped melt features could be observed within the regions analysed and only a limited number of small pores were present and are likely to have resulted from the gas atomisation process used to manufacture the powder used.

The effect of v^* and h^* on the microstructure and VHN of EBM Ti–6Al–4V is summarised by the annotated process map in Fig. 8. The diagram presented here is an enlarged version of the process space delineated in Fig. 3. In addition to the polarised light metallographs corresponding mean VHN data, an example of a typical lack of fusion feature observed in the specimen produced using an

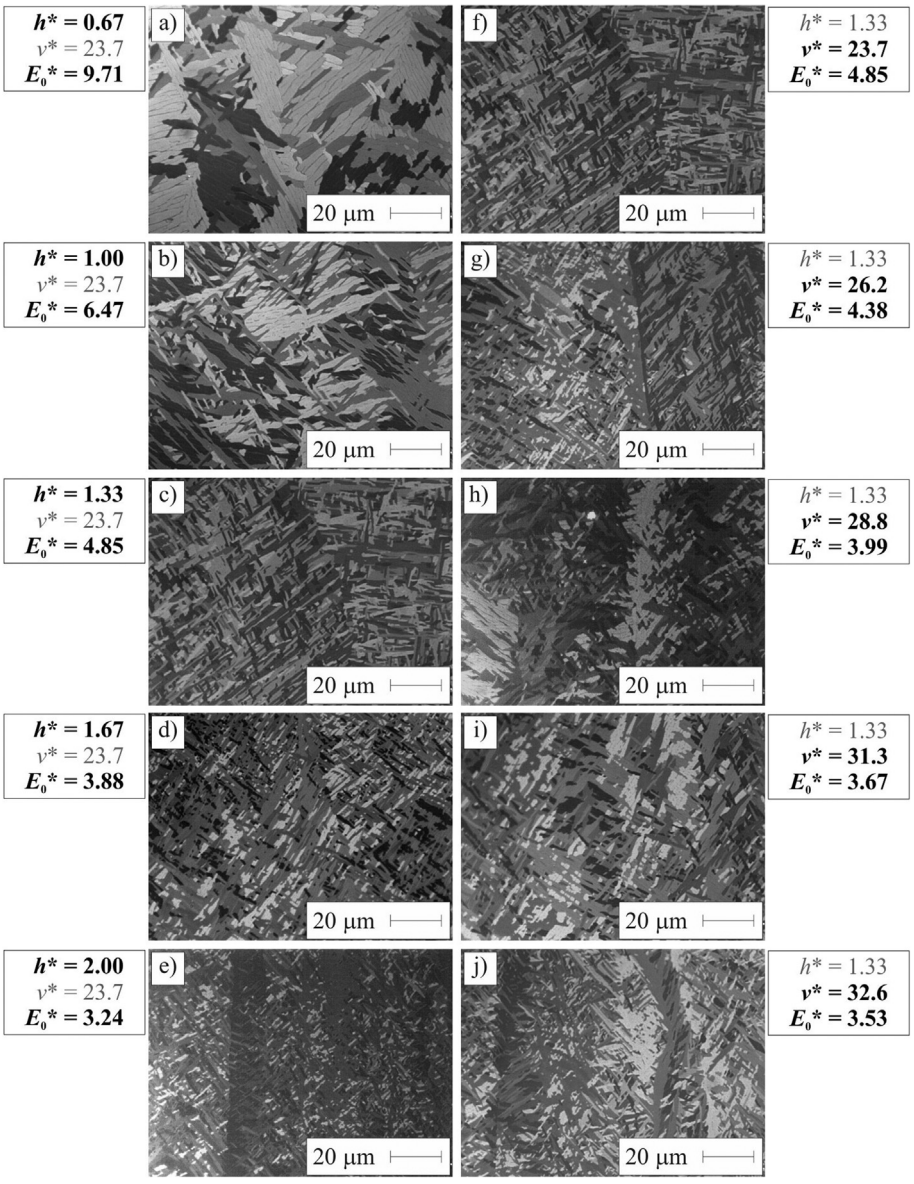

Fig. 4. Polarised light micrographs showing the effect of normalised hatch spacing, h^*, a) – e) and beam velocity, v^*, f) to j) on the microstructure of EBM Ti–6Al–4V. For clarity: In the left hand column, v^* is fixed and h^* varied, whilst h^* is fixed in the right hand column.

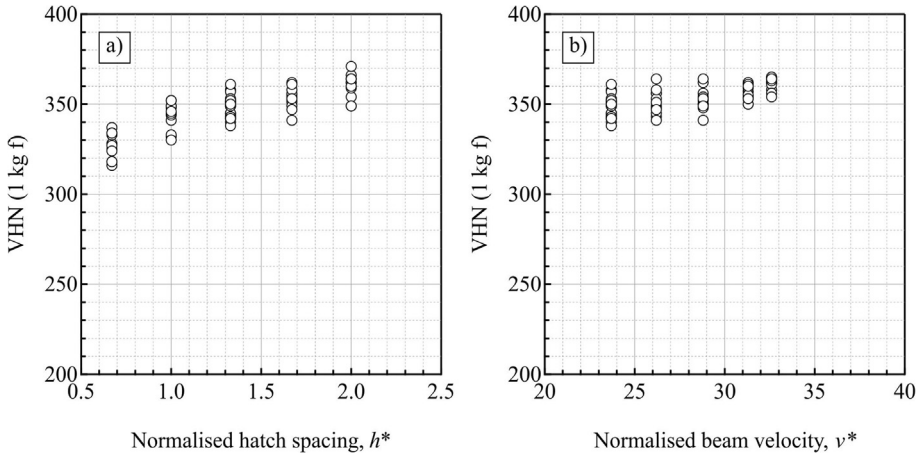

Fig. 5. The effect of a) normalised hatch spacing, h^* and b) beam velocity, v^* on the microhardness of EBM Ti–6Al–4V. All VHN data are shown.

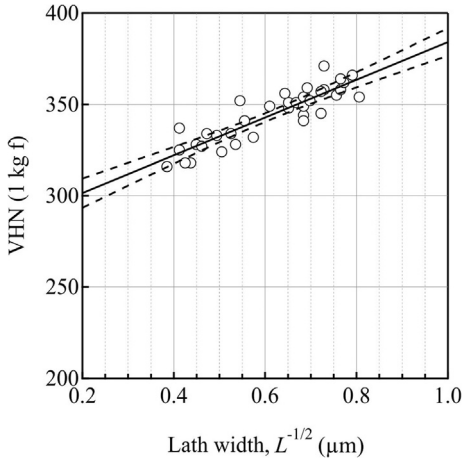

Fig. 6. Hall-Petch plot showing the general relationship between VHN and the measured alpha lath width, *L*. Dashed lines correspond to the 95% confidence intervals for the linear fitting coefficients.

EBM Ti–6Al–4V. Therefore, a thorough investigation will always be required to determine the borderline between acceptable and unacceptable microstructures, and to draw practical processing limits for alloys on diagrams such as that constructed in this study.

4. Conclusions

- By extending the approach outlined by Ion et al. [26], a method for constructing normalised processing diagrams for powder bed ALM has been discussed. Dimensionless groups of process variables applicable to ALM have been identified, and in conjunction with parameter data available in the literature, a practical process diagram has been constructed and its applicability has been investigated experimentally for powder bed EBM of Ti–6Al–4V.
- We have demonstrated that both the microstructure and undesirable feature population in EBM Ti–6Al–4V can be controlled through careful selection of processing parameters and that the general processing behaviour is consistent with

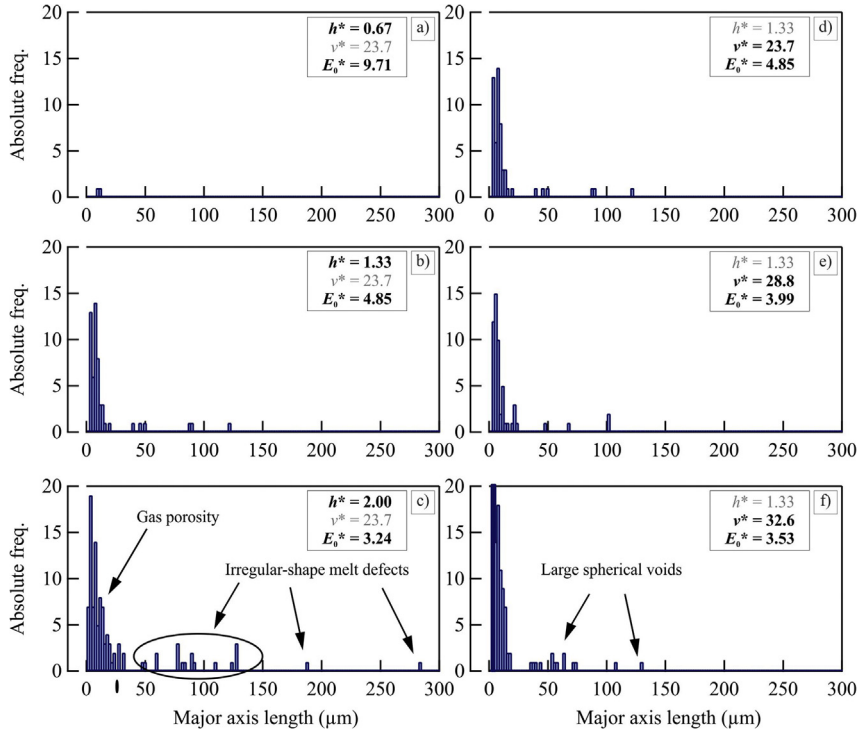

Fig. 7. Absolute frequency histograms illustrating the effect of h^*, a) – c) and v^*, d) – f) on the size and morphology of the sampled microstructural defect population. Measurements are taken from cross-section light microscopy.

h^* of 2, the highest value investigated in this study, is also appended to the process map. In the top right hand region, the combination of a small h^* and v^* leads to a relatively coarse, colony-type β_{tr} microstructure, a modest VHN and crucially, no observable microstructural anomalies within the examined cross-section. Processing in this region ($E_0^* \rightarrow 10$) is slow relative to the bottom-left corner of the process map ($3 < E_0^* < 4$), where high values of v^* and h^* lead to a more efficient process. Structural integrity is compromised in this region however, by the presence of undesirable microstructural feature such as lack of fusion defects, in spite of having a considerably higher VHN, and the critical lower bound E_0^* determined in this study aligns closed with that reported by Juechter et al. [8] for that reported for laser ALM of Ti–6Al–4V along with Stainless Steels and Nickel-base alloys.

- The diagrams proposed in this paper are intended to provide a practical framework for comparing and classifying the extensive range of ALM platforms, alloys and processing parameter data available in the literature and, rather than as a predictive tool, they provide *a priori* information on microstructure.
- The parameter data from which the normalised processing diagram has been developed are for largely small and simple geometries, and future studies should attempt to incorporate the effects of thermal mass and more complex design features on microstructure and mechanical behaviour.

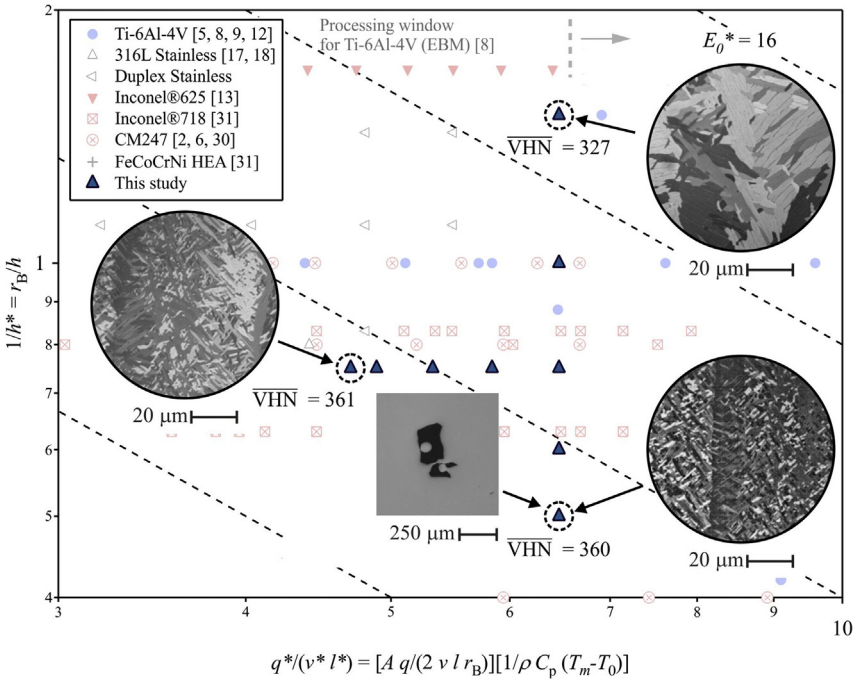

Fig. 8. Enlarged annotated process map of the region delineated in Fig. 3 summarising the microstructural response of EBM Ti–6Al–4V to systematic changes in normalised beam velocity, v^*, and hatch spacing, h^*. See Fig. 4 for the original polarised light metallographs. The mean VHN is also included.

- It is intended that these processing diagrams will provide useful insight to practising scientists and engineers for down-selecting the appropriate processing parameters for experimentation during early research and development programmes.

Acknowledgements

The current research was funded under the SAMULET II 10.4 programme (grants EP/H500383/1 and EP/H022309/1). The provision of materials and supporting information from Rolls-Royce plc is gratefully acknowledged by the authors together with the assistance provided by F. Derguti for specimen manufacture.

APPENDIX

Notation

A	surface absorptivity (–)
a	thermal diffusivity ($m^2\ s^{-1}$)
C_p	specific heat capacity ($J\ kg^{-1}\ K^{-1}$)
E^*	normalised volumetric energy density (–)
$E_0{}^*$	normalised equivalent energy density (–)
h	hatch spacing (m)
h^*	normalised hatch spacing (–)
L	alpha titanium lath width (μm)
L_m	latent heat of melting
λ	thermal conductivity ($W\ m^{-1}\ K^{-1}$)
ρ	density ($kg\ m^{-3}$)
q	power (W)
q^*	normalised power (–)
r_B	beam radius (m)
T	temperature (K)
T_m	melting temperature (K)
T_0	initial (or powder bed) temperature (K)
v	beam velocity ($m\ s^{-1}$)
v^*	normalised beam velocity (–)

References

[1] X. Gong, T. Anderson, K. Chou, Review on powder-based electron beam additive manufacturing technology, Manuf. Rev. 1 (2014) 2.
[2] L.N. Carter, M.M. Attallah, R.C. Reed, Laser powder bed fabrication of nickel-base superalloys: influence of parameters; characterisation, quantification and mitigation of cracking, Superalloys (2012) 577–586. John Wiley & Sons, Inc.
[3] B.E. Carroll, T.A. Palmer, A.M. Beese, Anisotropic tensile behavior of Ti–6Al–4V components fabricated with directed energy deposition additive manufacturing, Acta Mater. 87 (2015) 309–320.
[4] H. Qi, M. Azer, A. Ritter, Studies of standard heat treatment effects on microstructure and mechanical properties of laser net shape manufactured INCONEL 718, Metall. Mater. Trans. A 40 (2009) 2410–2422.
[5] W. Xu, M. Brandt, S. Sun, J. Elambasseril, Q. Liu, K. Latham, K. Xia, M. Qian, Additive manufacturing of strong and ductile Ti–6Al–4V by selective laser melting via in situ martensite decomposition, Acta Mater. 85 (2015) 74–84.
[6] L.N. Carter, C. Martin, P.J. Withers, M.M. Attallah, The influence of the laser scan strategy on grain structure and cracking behaviour in SLM powder-bed fabricated nickel superalloy, J. Alloys Compd. 615 (2014) 338–347.
[7] S.S. Al-Bermani, M.L. Blackmore, W. Zhang, I. Todd, The origin of microstructural diversity, texture, and mechanical properties in electron beam melted Ti-6Al-4V, Metall. Mater. Trans. A 41 (2010) 3422–3434.
[8] V. Juechter, T. Scharowsky, R.F. Singer, C. Körner, Processing window and evaporation phenomena for Ti–6Al–4V produced by selective electron beam melting, Acta Mater. 76 (2014) 252–258.
[9] C. Qiu, N.J.E. Adkins, M.M. Attallah, Microstructure and tensile properties of selectively laser-melted and of HIPed laser-melted Ti–6Al–4V, Mater. Sci. Eng. A 578 (2013) 230–239.
[10] S. Tammas-Williams, H. Zhao, F. Léonard, F. Derguti, I. Todd, P.B. Prangnell, XCT analysis of the influence of melt strategies on defect population in Ti–6Al–4V components manufactured by selective electron beam melting, Mater. Charact. 102 (2015) 47–61.
[11] X. Tan, Y. Kok, Y.J. Tan, M. Descoins, D. Mangelinck, S.B. Tor, K.F. Leong, C.K. Chua, Graded microstructure and mechanical properties of additive manufactured Ti–6Al–4V via electron beam melting, Acta Mater. 97 (2015) 1–16.
[12] B. Vrancken, L. Thijs, J.P. Kruth, J. Van Humbeeck, Microstructure and mechanical properties of a novel β titanium metallic composite by selective laser melting, Acta Mater. 68 (2014) 150–158.
[13] D.E. Cooper, N. Blundell, S. Maggs, G.J. Gibbons, Additive layer manufacture of Inconel 625 metal matrix composites, reinforcement material evaluation, J. Mater. Process. Technol. 213 (2013) 2191–2200.
[14] W.J. Sames, K.A. Unocic, R.R. Dehoff, T. Lolla, S.S. Babu, Thermal effects on microstructural heterogeneity of Inconel 718 materials fabricated by electron beam melting, J. Mater. Res. 29 (2014) 1920–1930.
[15] N.J. Harrison, I. Todd, K. Mumtaz, Reduction of micro-cracking in nickel

superalloys processed by selective laser melting: a fundamental alloy design approach, Acta Mater. 94 (2015) 59–68.
[16] L.N. Carter, X. Wang, N. Read, R. Khan, M. Aristizabal, K. Essa, M.M. Attallah, Process optimisation of selective laser melting using energy density model for nickel based superalloys, Mater. Sci. Technol. (2015), http://dx.doi.org/10.1179/1743284715Y.0000000108.
[17] C. Kamath, B. El-dasher, G.F. Gallegos, W.E. King, A. Sisto, Density of additively-manufactured, 316L SS parts using laser powder-bed fusion at powers up to 400 W, Int. J. Adv. Manuf. Technol. 74 (2014) 65–78.
[18] G. Ziółkowski, E. Chlebus, P. Szymczyk, J. Kurzac, Application of X-ray CT method for discontinuity and porosity detection in 316L stainless steel parts produced with SLM technology, Archives Civ. Mech. Eng. 14 (2014) 608–614.
[19] C. Qiu, C. Panwisawas, M. Ward, H.C. Basoalto, J.W. Brooks, M.M. Attallah, On the role of melt flow into the surface structure and porosity development during selective laser melting, Acta Mater. 96 (2015) 72–79.
[20] P. Nie, O.A. Ojo, Z. Li, Numerical modeling of microstructure evolution during laser additive manufacturing of a nickel-based superalloy, Acta Mater. 77 (2014) 85–95.
[21] S.L. Semiatin, V. Seetharaman, I. Weiss, Hot workability of titanium and titanium aluminide alloys—an overview, Mater. Sci. Eng. A 243 (1998) 1–24.
[22] S.L. Semiatin, G.D. Lahoti, Deformation and unstable flow in hot forging of Ti-6Ai-2Sn-4Zr-2Mo-0.1Si, MTA 12 (1981) 1705–1717.
[23] D. Dye, O. Hunziker, R.C. Reed, Numerical analysis of the weldability of superalloys, Acta Mater. 49 (2001) 683–697.
[24] P.A. Kobryn, S.L. Semiatin, Microstructure and texture evolution during solidification processing of Ti–6Al–4V, J. Mater. Process. Technol. 135 (2003) 330–339.
[25] M. Gäumann, C. Bezençon, P. Canalis, W. Kurz, Single-crystal laser deposition of superalloys: processing–microstructure maps, Acta Mater. 49 (2001) 1051–1062.
[26] J.C. Ion, H.R. Shercliff, M.F. Ashby, Diagrams for laser materials processing, Acta Metall. Mater. 40 (1992) 1539–1551.
[27] S. Bontha, N.W. Klingbeil, P.A. Kobryn, H.L. Fraser, Thermal process maps for predicting solidification microstructure in laser fabrication of thin-wall structures, J. Mater. Process. Technol. 178 (2006) 135–142.
[28] S.S. White, R. Bakish, in: R. Bakish (Ed.), Introduction to Electron Beam Technology, Wiley, New York, 1962, p. 225.
[29] B. Vrancken, L. Thijs, J.-P. Kruth, J. Van Humbeeck, Heat treatment of Ti6Al4V produced by selective laser melting: microstructure and mechanical properties, J. Alloys Compd. 541 (2012) 177–185.
[30] J. Boswell, Development of Aero Engine Component Manufacturing Using Laser Additive Manufacturing, MERLIN Final Report, 2014, http://cordis.europa.eu/docs/results/266/266271/final1-dr75-merlin-final-report.pdf.
[31] Y. Brif, M. Thomas, I. Todd, The use of high-entropy alloys in additive manufacturing,, Scr. Mater. 99 (2015) 93–96.
[32] R.J. Moat, A.J. Pinkerton, L. Li, P.J. Withers, M. Preuss, Crystallographic texture and microstructure of pulsed diode laser-deposited Waspaloy, Acta Mater. 57 (2009) 1220–1229.
[33] G. Lutjering, J.C. Williams, Titanium, Springer, 2007.
[34] D. Banerjee, J.C. Williams, Perspectives on titanium science and technology, Acta Mater. 61 (2013) 844–879.
[35] N. Hrabe, T. Quinn, Effects of processing on microstructure and mechanical properties of a titanium alloy (Ti–6Al–4V) fabricated using electron beam melting (EBM), part 1: distance from build plate and part size, Mater. Sci. Eng. A 573 (2013) 264–270.
[36] M. Thomas, T. Lindley, D. Rugg, M. Jackson, The effect of shot peening on the microstructure and properties of a near-alpha titanium alloy following high temperature exposure,, Acta Mater. 60 (2012) 5040–5048.
[37] W.S. Rasband, ImageJ, U.S. National Institute of Health, Maryland, USA, 1997-2012. http://imagej.nih.gov/ij.
[38] P.C. Collins, B. Welk, T. Searles, J. Tiley, J.C. Russ, H.L. Fraser, Development of methods for the quantification of microstructural features in α+β-processed α/β titanium alloys, Mater. Sci. Eng. A 508 (2009) 174–182.
[39] S.L. Semiatin, T.R. Bieler, The effect of alpha platelet thickness on plastic flow during hot working of TI–6Al–4V with a transformed microstructure, Acta Mater. 49 (2001) 3565–3573.
[40] H.M. Flower, Microstructural development in relation to hot working of titanium alloys, Mater. Sci. Technol. 6 (1990) 1082–1092.
[41] Materials Properties Handbook: Titanium Alloys, ASM International, Materials Park, OH, 1994.
[42] Metals Handbook, tenth ed. vol. 1, ASM International, Materials Park, OH, 1990.
[43] Metals Handbook, tenth ed. vol. 2, ASM International, Materials Park, OH, 1990.
[44] K. Mukai, Z. Li, L. Fang, Measurement of the densities of nickel-based ternary, quaternary and commercial alloys, Mater. Trans. 45 (2004) 2987–2993.
[45] L. Avala, M. Bheema, P.K. Singh, R.K. Rai, S. Srivastava, Int. J. Mech. Eng. Robotics 1 (2013) 2321–5747.